

RESEARCH ARTICLE | *Sensory Processing*

# M current regulates firing mode and spike reliability in a collision-detecting neuron

 **Richard B. Dewell**<sup>1</sup> and  **Fabrizio Gabbiani**<sup>1,2</sup>

<sup>1</sup>*Department of Neuroscience, Baylor College of Medicine, Houston, Texas; and* <sup>2</sup>*Department of Electrical and Computer Engineering, Rice University, Houston, Texas*

Submitted 1 June 2018; accepted in final form 18 July 2018

**Dewell RB, Gabbiani F.** M current regulates firing mode and spike reliability in a collision-detecting neuron. *J Neurophysiol* 120: 1753–1764, 2018. First published July 25, 2018; doi:10.1152/jn.00363.2018.—All animals must detect impending collisions to escape and reliably discriminate them from nonthreatening stimuli, thus preventing false alarms. Therefore, it is no surprise that animals have evolved highly selective and sensitive neurons dedicated to such tasks. We examined a well-studied collision-detection neuron in the grasshopper (*Schistocerca americana*) using in vivo electrophysiology, pharmacology, and computational modeling. This lobula giant movement detector (LGMD) neuron is excitable by inputs originating from each ommatidia of the compound eye. It possesses many intrinsic properties that increase its selectivity to objects approaching on a collision course, including switching between burst and nonburst firing. In this study, we demonstrate that the LGMD neuron exhibits a large M current, generated by noninactivating K<sup>+</sup> channels, that shortens the temporal window of dendritic integration, regulates a firing mode switch between burst and isolated spiking, increases the precision of spike timing, and increases the reliability of spike propagation to downstream motor centers. By revealing how the M current increases the LGMD's ability to detect impending collisions, our results suggest that similar channels may play an analogous role in other collision detection circuits.

**NEW & NOTEWORTHY** The ability to reliably detect impending collisions is a critical survival skill. The nervous systems of many animals have developed dedicated neurons for accomplishing this task. We used a mix of in vivo electrophysiology and computational modeling to investigate the role of M potassium channels within one such collision-detecting neuron and show that through regulation of burst firing and enhancement of spiking reliability, the M current increases the ability to detect impending collisions.

burst firing; collision avoidance; lobula giant movement detector; M current; spike timing

## INTRODUCTION

Failure to detect an impending collision can have serious, even fatal, consequences. Thus one might expect that neural circuitry dedicated to this task would be highly sensitive. Yet, much of the visual cues of an impending collision are shared by nonthreatening stimuli, including optic flow, approaching objects on a miss trajectory, or approaching objects slowing to a

stop. For this reason, neural circuitry dedicated to detecting impending collisions also needs to be highly selective.

One of the ways that sensory neurons can be both sensitive and selective is to use multiple firing modes. By multiplexing tonic and burst spiking, neurons increase their ability to both detect and discriminate, or to encode sensory information with both sensitivity and selectivity (Krahe and Gabbiani 2004; Sherman 2001). The use of burst and nonburst spiking as distinct firing modes has been demonstrated in contexts as diverse as audition in crickets, vision in flies, the electrosensory system of weakly electric fish, and the mammalian lateral geniculate nucleus of the thalamus (Allen and Marsat 2018; Clarke et al. 2015; Lesica and Stanley 2004; Longden et al. 2017; Marsat and Pollack 2006). In these systems, changes in a neuron's firing mode signify a change between detection and discrimination. In the detection mode, sensitivity is increased by the generation of a burst of spikes in response to a sudden or novel change in the stimulus. In the discrimination mode, selectivity is increased by encoding stimulus details in the temporal pattern of spikes. The switch between these modes can depend on both intrinsic membrane properties and changes in network activity (Krahe and Gabbiani 2004; Sherman 2001).

Intrinsic neuronal mechanisms involved in switching firing mode include K<sup>+</sup> conductances, such as the M current (Battefeld et al. 2014; Deemyad et al. 2011; Golomb et al. 2006; Yue and Yaari 2004). The M current, generated by KCNQ/Kv7 channels, is a voltage-dependent, noninactivating K<sup>+</sup> current involved in numerous aspects of neuronal function that is evolutionarily conserved in worms, insects, and mammals (Cavaliere and Hodge 2011; Greene and Hoshi 2017; Wei et al. 2005). Initial characterizations of the M current showed a slow depolarization of the postsynaptic membrane potential following activation of muscarinic acetylcholine receptors caused by deactivation of an M current (Adams and Brown 1982; Brown and Adams 1980). Postsynaptically, the M current contributes to spike frequency adaptation and dendritic integration (Delmas and Brown 2005; Hu et al. 2007; Shah et al. 2011). More recently, a high density of KCNQ channels has been found in the axon and synaptic terminals of various neuron types (Battefeld et al. 2014; Devaux et al. 2004; Huang and Trussell 2011; Vervaeke et al. 2006). These channels contribute to the resting membrane potential (RMP) and diminish excitability (Battefeld et al. 2014; Huang and Trussell 2011; Schwarz et al. 2006).

Address for reprint requests and other correspondence: F. Gabbiani, Dept. of Neuroscience, One Baylor Plaza, Houston, TX 77030 (e-mail: gabbiani@bcm.edu).

To explore the neuronal effects of the M current on the responses of collision-detecting circuits, we used an identified neuron in locusts that shows both high sensitivity to small visual objects (Rowell et al. 1977) and selectivity for visual stimuli mimicking impending collision (Rind and Simmons 1992; Schlotterer 1977): the lobula giant movement detector neuron (LGMD; O'Shea and Williams 1974). The LGMD integrates inputs originating from every facet of the compound eye, and despite activation of individual facets reliably triggering spiking (Jones and Gabbiani 2010), it responds selectively to (simulated) approaching objects that activate thousands of facets on the basis of the object's trajectory and spatial coherence (Dewell and Gabbiani 2018; Gray et al. 2001). The descending contralateral movement detector (DCMD; O'Shea and Williams 1974) relays the firing pattern of the LGMD to motor centers in the meso- and metathoracic ganglia that initiate and control escape behaviors. Different aspects of these firing patterns, including burst firing, have been tied to the generation of escape behaviors (Dewell and Gabbiani 2018; Fotowat et al. 2011; McMillan and Gray 2015).

In the present study we employ this well-characterized neural system with a clear behavioral role to investigate the role of the M current in the sensory encoding of threatening visual stimuli. Using a mix of *in vivo* electrophysiology, pharmacology, and computational modeling, we demonstrate that the M conductance  $g_M$  narrows the window of dendritic integration by decreasing temporal summation, regulates a firing mode switch between burst and isolated spiking, increases the precision of spike timing, and increases the reliability of spike propagation. Combined, these features are expected to increase the LGMD's ability to encode the sensory features of approaching objects and help locusts avoid predation.

## MATERIALS AND METHODS

**Animals.** All experiments were performed on adult grasshoppers 7–12 wk of age (*Schistocerca americana*). Animals were reared in a crowded laboratory colony under 12:12-h light-dark conditions. For experiments, preference was given to larger females ~3 wk after final molt that were alert and responsive. Animals were selected for health and size without randomization, and investigators were not blinded to experimental conditions. Sample sizes were not predetermined before experiments. The surgical procedures used have been described previously (Dewell and Gabbiani 2018; Gabbiani and Krapp 2006; Jones and Gabbiani 2012). Briefly, following a dissection that exposed the posterior surface of the right optic lobe, the brain and optic lobe were held in fixed position, and *in vivo* electrophysiological recordings of the LGMD were conducted. The LGMD was identified by the coincidence of its spiking with that of the DCMD and its unique morphology (O'Shea and Williams 1974), visualized by intracellular injection of Alexa Fluor 594 hydrazide salt through a stereomicroscope (Invitrogen, Thermo Fisher Scientific, Carlsbad, CA).

**Visual stimuli.** Visual stimuli were generated using MATLAB and Psychtoolbox-3 (PTB-3) on a personal computer running Windows XP. A conventional cathode ray tube monitor refreshed at 200 frames/s was used for stimulus display (LG Electronics, Seoul, Korea). Looming stimuli were the two-dimensional projections on a screen of an object approaching on a collision course with the animal. They consisted of dark squares simulating the approach of a solid object with half size  $l$  and constant approach speed  $v$ , characterized by the ratio  $l/v$  (see *top inset* in Fig. 3A), as previously described (Gabbiani et al. 2001).

**Electrophysiology.** Extracellular recordings of the DCMD were carried out with a pair of Formvar-coated stainless steel wire hooks placed on the ventral nerve cord between the subesophageal and prothoracic ganglia (Gabbiani et al. 2001). The DCMD recordings were bandpass filtered from 100 and 5,000 Hz and digitized at 10,036.5 Hz.

Sharp electrode LGMD intracellular recordings were carried out in current-clamp mode using thin-walled borosilicate glass pipettes (outer/inner diameter: 1.2/0.9 mm; WPI, Sarasota, FL; see Jones and Gabbiani 2012 as well as Dewell and Gabbiani 2018 for details). After amplification, intracellular signals were low-pass filtered (cutoff frequency: 10 kHz for the membrane potential,  $V_m$ , and 5 kHz for the membrane current,  $I_m$ ) and digitized at a sampling rate of 20,073 Hz. We used a single electrode clamp amplifier capable of operating in discontinuous mode at high switching frequencies (typically ~25 kHz; SEC-10, NPI, Tamm, Germany). Responses to current injections were recorded in discontinuous current-clamp mode (DCC). For two animals we conducted dual recordings (see Fig. 4C) by inserting a second sharp electrode into the excitatory dendritic field of the LGMD (Fig. 1A) with a motorized micromanipulator (Sutter Instruments, Novato, CA). Recordings were made in bridge or DCC mode with a second SEC-10 amplifier. Switching frequencies, signal filtering, and digitization were the same for both recordings.

Injected currents consisted of steps (1–2 s in duration), waveforms producing simulated excitatory postsynaptic potentials (sEPSPs), and chirp currents (see below). sEPSPs were generated by injecting five current waveforms with a set delay between them varied between 5 and 20 ms. Each waveform,  $I(t)$ , had a time course resembling that of an excitatory postsynaptic current,

$$I(t) = A(1 - e^{-t/\tau_1})e^{-t/\tau_2},$$

with peak amplitude  $A$ , rising time constant  $\tau_1 = 0.3$  ms, and falling time constant  $\tau_2 = 3.0$  ms. Membrane potential summation was calculated as the ratio  $(p_5 - p_1)/p_1$ , with  $p_1$  and  $p_5$  being the peak amplitude of the membrane potential relative to rest during the first and fifth sEPSPs. We measured the sEPSP input resistance by dividing the integrated membrane potential (relative to rest) by the integrated input current (charge), giving a value (in units of mV·ms/nA·ms = M $\Omega$ ) that is readily comparable to the input resistance recorded in response to current pulses.

Chirp currents are sine waves of increasing frequency. They allow rapid probing of the frequency response of a neuron. If the chirp current is defined as  $I(t) = I_p \sin \phi(t)$ , where  $I_p$  is the peak current and  $\phi(t)$  is the phase of the sine wave, then its instantaneous frequency is defined as  $f(t) = (1/2\pi)(d\phi/dt)$  (in Hz). Note that if  $\phi(t) = 2\pi vt$ , the frequency is constant:  $f(t) = v$ . We used chirps with a duration of 20 s that increased in frequency either linearly or exponentially with time. Exponential frequency sweeps were used in most experiments, as well as for all simulations, because they yielded a more even distribution over time of the frequencies included in the chirp. The linear chirp started at 0 Hz and was calculated as  $I(t) = I_p \sin \pi\beta t^2$ , where  $t$  is the time from the start of the chirp (in s) and  $\beta$  is the rate of increase in instantaneous chirp frequency (in Hz/s). The exponential chirp was given by  $I(t) = I_p \sin \pi f_0 t e^{\beta t}$ , where  $f_0$  is the initial chirp frequency and  $\beta$  determines the (accelerating) rate of frequency increase (Barrow and Wu 2009). For all exponential chirps, we used  $f_0 = 0.05$  Hz and  $\beta = 0.24$  Hz, which produced a chirp current increasing to 35 Hz over 20 s. To rule out phase delays between the computer-generated waveform and the current injected by the amplifier, we recorded simultaneously for all chirps the injected membrane current and the membrane potential. We used these recordings for data analysis to prevent any timing delays in the generation of the chirp currents from skewing results.

**Pharmacology.** We applied the M channel blocker 10,10-bis(4-pyridinylmethyl)-9(10H)-antracene (XE991) either directly in the bath saline or by local puffing. For local puffing, drugs were mixed with physiological saline containing fast green (0.5%) to visually

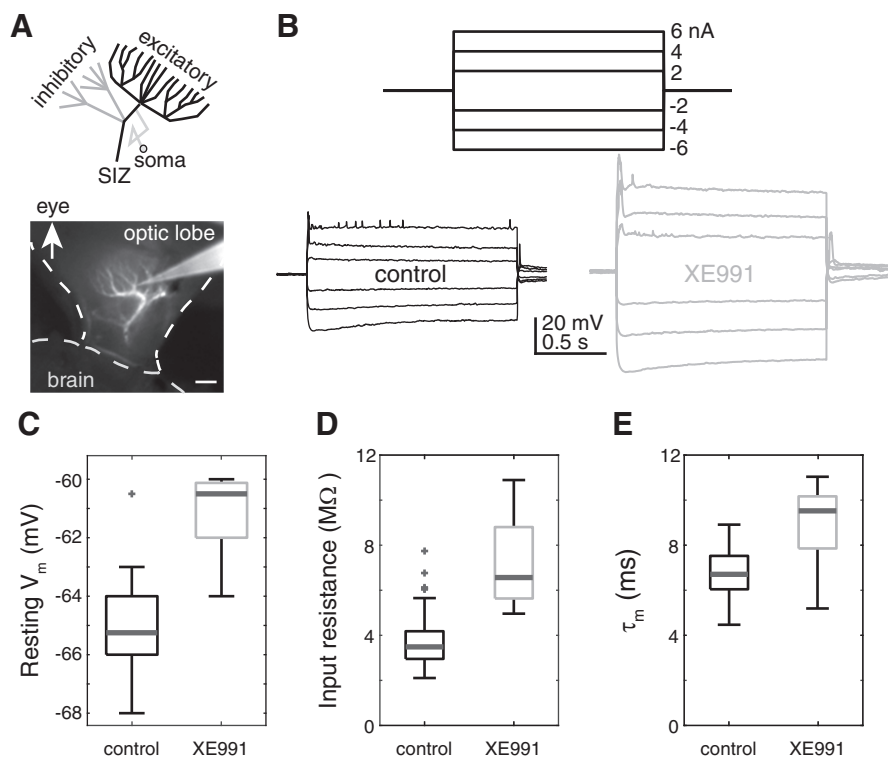


Fig. 1. Intracellular lobula giant movement detector (LGMD) recordings reveal a resting M conductance ( $g_M$ ). *A*, top: a schematic illustration of the LGMD. The recordings were taken from the region illustrated in black. SIZ, spike initiation zone. *Bottom*, a micrograph of the LGMD stained with Alexa 594 and the intracellular recording pipette. Scale bar, 100  $\mu\text{m}$ . *B*: current steps were injected before (*left*) and after (*right*) application of the  $g_M$  blocker XE991. Both hyperpolarizing and depolarizing currents generated larger changes in membrane potential after  $g_M$  blockade. Traces have been median filtered to remove spikes. *C*: resting membrane potential ( $V_m$ ) increased after  $g_M$  blockade by XE991 ( $P = 0.0013$ ; control, 11 recordings from 8 animals; XE991, 12 recordings from 8 animals). *D*: input resistance increased after  $g_M$  blockade by XE991 ( $P = 1.9 \times 10^{-7}$ ; control, 79 recordings from 59 animals; XE991, 13 recordings from 8 animals). *E*: membrane time constant ( $\tau_m$ ) increased after  $g_M$  blockade by XE991 ( $P = 4.3 \times 10^{-4}$ ; control, 83 recordings from 59 animals; XE991, 13 recordings from 8 animals). In *C–E*, central lines are medians, top and bottom box edges are 75th and 25th percentiles, whiskers denote the extent of data up to 1.5 times the interquartile range, and crosses denote outliers.

monitor the affected region. They were puffed using a micropipette connected to a pneumatic picopump (PV830; WPI). For bath applications, we used XE991 at concentrations of 200–400  $\mu\text{M}$ , and for local puffing, we used a concentration of 6 mM in the pipette. Based on previous calculations, this produced concentrations of  $\sim 100$ –200  $\mu\text{M}$  in the lobula (Dewell and Gabbiani 2018). The LGMD axon travels through the protocerebrum in the brain, with its synaptic terminals located  $>500$   $\mu\text{m}$  from our puff pipette in the lobula. Our results suggest that M channels extend through the axon, and consequently these channels would be exposed to  $<100$   $\mu\text{M}$  XE991. In pilot experiments, effects of M current block by XE991 were observed with lobula concentrations  $<30$   $\mu\text{M}$ , but the full effects described in the current experiments required the higher concentration. Previous dosage response measurements have found XE991 to have partial effects at  $<10$   $\mu\text{M}$ , with complete block requiring  $\sim 100$   $\mu\text{M}$  (Battefeld et al. 2014; Cavaliere and Hodge 2011; Martire et al. 2004). We are unaware of any previous studies using XE991 in grasshoppers, but data from other species combined with the high evolutionary conservation of M channels (Wei et al. 2005) suggest that the data presented in this study are the result of complete blockade of M channels within the LGMD. The mechanisms by which XE991 blocks the M current are still under investigation. In isolated cultured cells, 10  $\mu\text{M}$  XE991 was found to only block activated subunits with little effectiveness near RMP (Greene et al. 2017). In this study we found that XE991 decreased  $g_M$  at RMP, as has been found in other neurons (Guan et al. 2011). This difference might be due to the modulatory state of the channels or differences in drug concentration. Although XE991 is selective for M channels, partial block of other  $\text{K}^+$  channels by XE991 has been demonstrated in cultured cells, with 100  $\mu\text{M}$  XE991 reducing Kv2.1 currents by  $\sim 20\%$  in human embryonic kidney cells (Wladyka and Kunze 2006) and reducing ERG1–2 currents by  $\sim 20$ –50% in *Xenopus* oocytes (Elmedy et al. 2007). It is unknown whether the LGMD possesses these channel types or if they would be affected by these concentrations of XE991 in vivo. In one animal, data were collected after washing of XE991, which required  $>30$  min of rinsing with fresh saline. In this preparation, all measurements returned to control levels including 100% DCMD spike propagation and normal spike timing (see RESULTS).

The addition of XE991 reduced excitatory synaptic inputs impinging on the LGMD (see DISCUSSION). To test whether this could explain any of the reported effects, we blocked synaptic inputs with mecamylamine. After mecamylamine application, the RMP was  $-65.3 \pm 1.2$  mV, temporal summation was unchanged, burst firing was not increased, and spike timing was not more variable. In each of these cases, the effects of mecamylamine were not significant and in the opposite direction of those of XE991. Mecamylamine increased the LGMD input resistance and membrane time constant by  $\sim 5\%$ , but this change is much smaller than that produced by XE991 (see Fig. 2, *D* and *E*).

**Data analysis and statistics.** Data analysis was carried out with custom MATLAB code (The MathWorks, Natick, MA). Linear fits were done by minimization of the sum of squared errors. Exponential fits were made with the MATLAB function “lsqcurvefit,” which minimizes the least squared error between the data and fitting function. Goodness of fit was denoted by  $R^2$ , calculated as 1 minus the sum of the squared errors of the fit divided by the sum of the squared deviation from the mean of the data. Small hyperpolarizing step currents were used for calculating the input resistance and the membrane time constant. The membrane time constant was calculated by fitting a single exponential to the membrane potential for the period from 0.5 to 13.0 ms after the start of hyperpolarizing current injection.

Unless otherwise specified, all statistical tests were made using the Wilcoxon rank sum test (WRS), which does not assume normality or equality of variance. For any tests that assumed normality, data were first assessed using a Lilliefors test. For displaying summary data, average values were given as median and variance was displayed as median average deviation (mad). For linear fits, the reported  $r$  and  $P$  values were calculated from the Pearson linear correlation coefficient, testing its statistical difference from zero.

For box plots, the center line shows the median, the upper and lower box limits mark the 25th and 75th percentile of the distribution, respectively, and the whiskers above and below each box extend 1.5 times the interquartile range up to the minimum and maximum values. Points beyond the whiskers mark outliers.

The timing of spikes was calculated on the basis of their peak for both intracellular and extracellular recordings. During chirp currents,

spike phases were calculated relative to the peaks of the sine wave, defined as  $0^\circ$ , with negative phases on the rising portion of the sine wave and positive phases on the falling portion. With the use of MATLAB, this was implemented by applying the function “acosd” (inverse cosine between  $0^\circ$  and  $180^\circ$ ) to the normalized chirp current,  $I(t)/I_p$ , at the time of a spike, multiplied by  $-1$  times the sign of the first derivative of the chirp current at the time of the spike. The corresponding spike time relative to the time of  $0^\circ$  phase was calculated by dividing the phase by  $360^\circ$  and by the instantaneous chirp current frequency (in  $s^{-1}$ ). The instantaneous chirp frequency was calculated by approximating numerically the first derivative of  $\sin^{-1}I(t)/I_p$  divided by  $2\pi$ . Spike phase coherence was calculated as  $1$  minus the variance of  $e^{i\Phi}$ , where  $i = \sqrt{-1}$  and  $\Phi$  is the vector of all spike phases (in radians, scaled from  $-\pi$  to  $\pi$ ; Sinha and Narayanan 2015). To calculate the  $0^\circ$  phase crossing for each recording, a least-squared-error linear fit was calculated between the instantaneous chirp frequencies and the spike phases of that recording (see Fig. 4D).

To calculate the reliability of the LGMD-to-DCMD spike propagation, we identified DCMD spikes by their peak height from extracellular recordings. For most DCMD recordings, the DCMD spikes are much larger than those of other neurons in the nerve cord. In noisy nerve cord recordings, some DCMD spikes were not clearly separable from those of other axons during high-frequency firing. In these cases, we preferred to exclude DCMD spikes over inclusion of possible non-DCMD spikes. Once DCMD spikes were identified, we iteratively examined each LGMD spike and checked for a matching DCMD spike following it by 1.3–4.8 ms. Previous paired DCMD recordings have shown a 1-ms synaptic delay between LGMD and DCMD spikes and  $\sim$ 1-ms axonal conduction time to the thoracic connective where we record them (O’Shea and Williams 1974; Rind 1984), so we chose the 1.3- to 4.8-ms range to include the expected delay plus a small buffer; in all control spikes the delay fell between 1.6 and 2.5 ms. To prevent a DCMD spike from being matched to two LGMD spikes with interspike interval (ISI)  $<$ 4.8 ms, DCMD spikes were removed upon matching. Even with the conservative thresholding, a paired DCMD spike was identified for 99.7% of LGMD spikes in control conditions, so a more inclusive analysis would have minimal effects on the findings. The DCMD spike probability was the percentage of LGMD spikes with matched DCMD spikes. After matching, the spike delay was the time from the peak of the LGMD spike to the peak of the DCMD spike.

**Neuronal modeling.** We adapted a recently developed model for the LGMD simulations, described in Dewell and Gabbiani (2018) and available for download from the ModelDB repository (accession code 195666). The M conductance density varied with neuron location as follows (all conductance values are for  $-65$  mV). The axon had a constant density of  $53 \mu S/cm^2$ , the spike initiation zone (SIZ) had a constant density of  $144 \mu S/cm^2$ , the primary neurite connecting the dendrites to the SIZ had conductance densities decreasing linearly with distance from the SIZ such that the compartment closest to the SIZ had a density of  $226 \mu S/cm^2$ , the compartment at the base of the excitatory dendrites had a density of  $79 \mu S/cm^2$ , and the average density was  $125 \mu S/cm^2$ . The two inhibitory dendritic subfields had a mean density of  $40 \mu S/cm^2$ , and the excitatory dendritic field had a mean density of  $17 \mu S/cm^2$  (see schematics in Fig. 6A). The channels were modeled with steady-state activation set by a Boltzmann function with half activation of  $-47$  mV and steepness of  $12$  mV, yielding a resting M conductance that was 13.1% of its peak conductance. There were no synaptic inputs or added membrane noise in the simulations. For data shown in Figs. 6 and 7, membrane properties were measured from 11 model compartments, all within  $150 \mu m$  ( $86 \pm 44 \mu m$ , mean  $\pm$  SD) of the base of the excitatory dendritic field. The model and code allowing reproduction of Figs. 6 and 7 are available on ModelDB (accession code 241169).

## RESULTS

**$g_M$  alters the electrotonic properties of the LGMD.** To test for the presence and role of  $g_M$  in the LGMD, sharp electrode intracellular recordings were employed in vivo before and after application of the specific  $g_M$  blocker XE991 (Fig. 1A). After blockade, immediate changes were seen in the passive electrotonic properties of the neuron, revealing both that M channels are present within the LGMD and that a significant number are open at rest. This was clear in the increased membrane potential change in response to both hyperpolarizing and depolarizing step currents (Fig. 1B). The RMP increased by  $\sim$ 4 mV from  $-65$  to  $-61$  mV after XE991 application (Fig. 1C). This increase brings the neuron closer to spike threshold and increased excitability. The median membrane input resistance increased by 88% after  $g_M$  blockade (Fig. 1D). A single exponential function was fit to the membrane potential for the time period immediately following the onset of each current step to measure the membrane time constant (as in Dewell and Gabbiani 2018). After  $g_M$  blockade, the median membrane time constant increased by 44% (Fig. 1E). Each of these changes to the electrotonic properties of the membrane after XE991 application suggests excitatory effects consistent with the removal of a  $K^+$  current.

**$g_M$  decreases summation of EPSPs in the LGMD.** The conductance  $g_M$  can reduce EPSP amplitude and summation, thereby lessening dendritic integration, as is the case, for example, in cortical neurons. To test if that is also the case in the LGMD, we injected brief, transient currents to simulate a series of five EPSPs at the level of the LGMD’s membrane potential. As shown previously, these simulated EPSPs (sEPSPs) summate sublinearly in the dendrites of the LGMD (Dewell and Gabbiani 2018). Blocking  $g_M$  with XE991 increased the amplitude and duration of the sEPSPs (Fig. 2A). In addition, the summation from the first to the fifth sEPSP increased after  $g_M$  block by an average of 75% (Fig. 2B). Dividing the mean sEPSP amplitude by the mean current injected yielded the effective input resistance to the sEPSP. This input resistance increased after  $g_M$  block (Fig. 2C) by an amount similar to that observed during current injection (cf. Fig. 1D). The increase in sEPSP amplitude and summation after  $g_M$  block shows that  $g_M$  reduces excitability to excitatory synaptic inputs.

**$g_M$  toggles the firing mode of the LGMD.** KCNQ channels can also alter the firing properties of a neuron, so we examined the influence of  $g_M$  on the spiking output of the LGMD and found dramatic changes. In response to objects approaching on a collision course or their two-dimensional projections, the LGMD generates a characteristic firing pattern. The spike rate ramps up as the stimulus expands, reaches a peak, and decays before the projected time of collision. Following the looming response there is a prolonged afterhyperpolarization. An example of the LGMD response to a looming stimulus is shown in Fig. 3A. In the control case, the usual response was observed. However, after XE991 application, the LGMD responded with bursts of activity, as shown in examples from two animals (Fig. 3A). The increase in burst firing was even more striking for depolarizing current steps. In control conditions, such current steps generated immediate firing with a rate that decayed exponentially (Fig. 3B, top; Gabbiani and Krapp

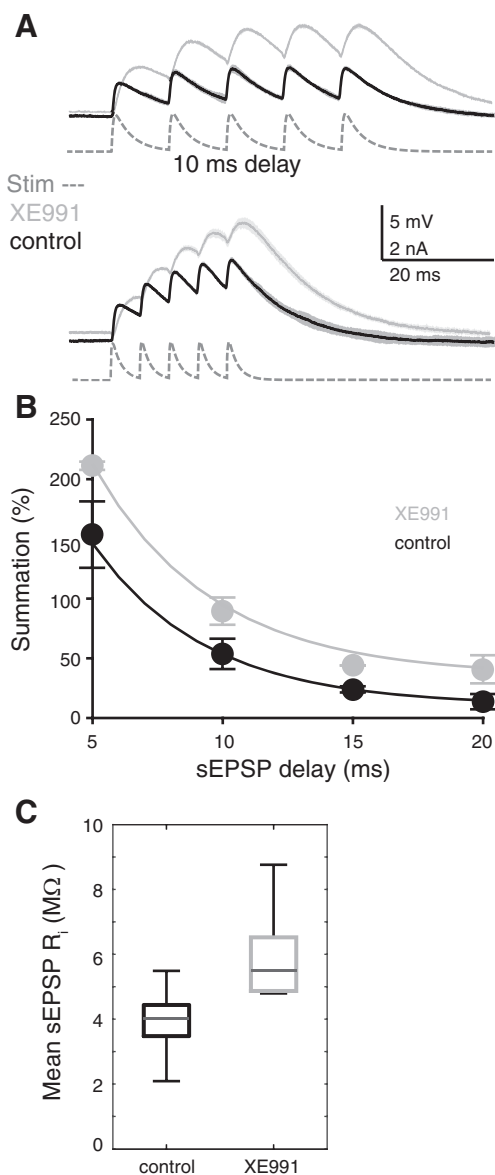


Fig. 2. Injection of simulated excitatory postsynaptic potential (sEPSP) currents shows that M conductance ( $g_M$ ) reduces temporal summation. *A*: example traces before (control) and after block of  $g_M$  with XE991. Each trace shows the lobula giant movement detector (LGMD) membrane potential in response to 5 sEPSP currents (dashed traces; Stim) with delays of either 5 (bottom) or 10 ms (top). After  $g_M$  blockade, the summation of these sEPSPs increased for both delays (measured as %change from peak of first to peak of fifth sEPSP). *B*: summation decreased exponentially with longer sEPSP delays. Summation was higher for delays of 5 ( $P = 0.006$ ), 10 ( $P = 0.001$ ), and 20 ms ( $P = 0.003$ ); data were recorded after XE991 application with a delay of 15 ms for only 1 animal. *C*: measuring the mean input resistance ( $R_i$ ) associated with sEPSP revealed a 50% increase in total sEPSP response after  $g_M$  blockade by XE991 ( $P = 3.5 \times 10^{-7}$ ). For *B* and *C*, control data originate from 10 recordings from 6 animals and XE991 data from 5 recordings from 3 animals. In *C*, central lines are medians, top and bottom box edges are 75th and 25th percentiles, and whiskers denote the extent of data.

2006; Peron and Gabbiani 2009a). After XE991 addition, however, the LGMD often generated rhythmic bursts of activity (Fig. 3*B*, bottom). Examination of the probability histogram of the ISIs showed a clear increase in spikes with ISIs around 4 ms (Fig. 3*C*). In five of eight animals an increase in bursting was seen ( $P < 0.001$ ), and on average, the fraction of spikes having ISIs of 2–5 ms increased from 2% to 38% (Fig. 3*D*).

$g_M$  improves the reliability of LGMD spiking. A shift in firing mode from isolated to burst spiking has been associated with a change in a neuron's operating regime from fine discrimination to detection. In the detection mode, whether or not spikes are present conveys the relevant information, whereas in the discrimination mode, specific stimulus parameters may be encoded in the temporal pattern of the spikes. How much information can be conveyed in the timing of spikes depends on their reliability. To test this reliability in the LGMD, we injected chirp currents (sine waves of increasing frequency; see MATERIALS AND METHODS) at depolarized holding potentials and measured the phase of the generated spikes (Fig. 4, *A* and *B*). For these measurements, spikes occurring at the peak and the trough of the input current were assigned phases of  $0^\circ$  and  $\pm 180^\circ$ , respectively. Negative and positive phases were assigned to spikes occurring on the rising and falling slope of the sinusoids, respectively (Fig. 4*A*). For low-frequency oscillating currents, spikes mostly came on the rising slope, while they fell on the falling slopes at high frequency (Fig. 4*C*). The measured spike phase was independent of recording location, as shown by the simultaneously recorded and overlaid traces in Fig. 4*C*. Hence, there was no noticeable propagation lag between simultaneously recorded locations across the excitatory dendritic field. The spike phase was consistent across animals (blue lines in Fig. 4*D*) and showed a clear progression with the input frequency of the chirp. On average, spikes were most synchronous with the input around theta frequency (zero crossing of blue lines in Fig. 4*D*). The consistency of spike timing was reflected in their spike phase coherence, which was high compared with that in other systems (Fig. 4*E*, gray bars; McLelland and Paulsen 2009; van Brederode and Berger 2008). The spike phase coherence was even higher within narrow frequency ranges; e.g., spikes during the 5- to 10-Hz period of the chirp had a spike phase coherence of 0.93. After addition of XE991, there was a reduction in spike phase coherence (Fig. 4*E*, green bars). To compare the absolute difference in spike timing, we plotted the time of each spike relative to the peak of the input current sinusoid ( $0^\circ$ ). In control data these spike times were tightly grouped around the sinusoid peak time with 65% of spikes occurring within  $\pm 10$  ms of it (Fig. 4*F*, gray bars). After XE991 application only 10% of spikes occurred in the same interval (Fig. 4*F*, green bars). This demonstrates that  $g_M$  increases the reliability of the LGMD's spike timing.

$g_M$  is critical for signal propagation from the LGMD to the DCMD. The block of  $g_M$  reduced not only the spike timing reliability within the LGMD but also the reliability of the signal propagation from the LGMD to its downstream target, the DCMD. Under control conditions, LGMD spikes faithfully generate spikes in the DCMD through a mixed chemical and electrical synapse (Killmann and Schürmann 1985; Rind 1984). We used simultaneous intracellular LGMD and extracellular DCMD recordings to measure how consistent this spike propagation was before and after  $g_M$  blockade. After XE991 application, spike failures occurred during both burst and isolated spiking (Fig. 5*A*). For control recordings, we detected matching DCMD spikes for 99.7% of LGMD spikes. Manual inspection of the recordings suggested that the 0.3% failure rate was due to limitations in detecting DCMD spikes from noisy extracellular recordings rather than genuine failure of the LGMD/DCMD synapse. Following  $g_M$  blockade, six of

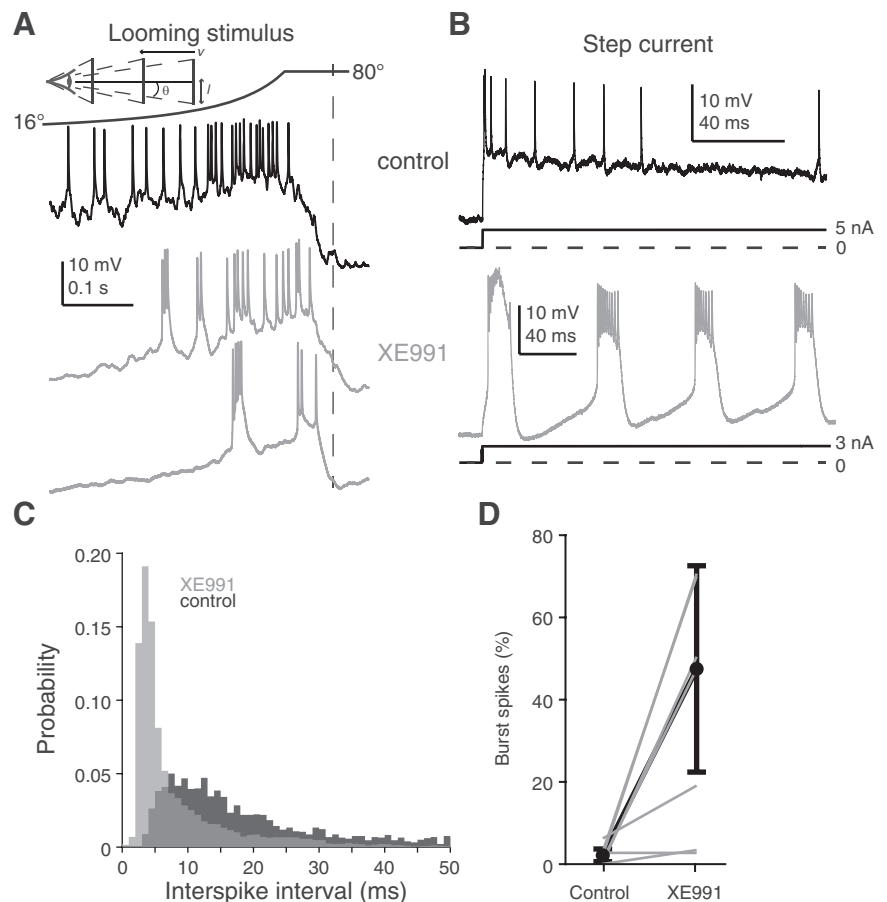


Fig. 3. Blockade of M conductance ( $g_M$ ) increased burst firing. **A**: example responses to looming stimuli ( $l/|v| = 50$  ms) before and after  $g_M$  blockade by XE991. *Top*, schematic of looming stimulus where  $l$  is half-size;  $v$  is approach speed, and  $\theta$  is half-angular subtense at the eye. Black line shows the nonlinear increase in angular subtense ( $2\theta$ ), characteristic of looming stimuli. *Bottom*, example responses from 2 animals after XE991 addition show an increase in bursting with clear pauses in firing that were not seen in control looming responses. Dashed vertical line indicates the projected time of collision. **B**: depolarizing step currents generated rhythmic bursting after application of XE991 instead of the isolated spikes generated in control. **C**: a probability histogram of the interspike intervals (ISIs) exhibits a large increase in intervals of  $\sim 4$  ms after XE991 addition. **D**: the prevalence of burst spikes (those with ISIs of 2–5 ms) increased after XE991. Gray lines show data from individual animals ( $n = 8$ ). Black lines show the population response; circles are medians, error bars are  $\pm$  median average deviation (mad). Analyses in **C** and **D** included 4,684 spikes for control and 14,865 spikes after XE991 application from 8 animals.

eight animals had a significant increase in failures of spike transmission to the DCMD, with only 63% of LGMD spikes initiating DCMD spikes, on average (Fig. 5B). During control conditions, reliable DCMD spike initiation occurs over a broad range of instantaneous LGMD firing frequencies (0–500 spikes/s), so the increase in firing rates after XE991 application cannot explain the failures.

We next measured the time lag from the peak of each LGMD action potential to the peak of the corresponding extracellular DCMD spike (Fig. 5C). In control conditions, DCMD spikes trailed those of the LGMD by  $\sim 2$  ms. After XE991 application, there was a significant increase in this delay in all animals (Fig. 5D). Not only did the delay increase, but its variability increased as well, approximately doubling from 0.17 to 0.37 ms (Fig. 5E). This shows that  $g_M$  increases the reliability of LGMD spike generation (Fig. 4, E and F) as well the reliability of their propagation to downstream motor centers.

*A multicompartmental model reproduced the subthreshold effects of  $g_M$ .* We adapted a recent biophysical model of the LGMD, illustrated in Fig. 6A, to investigate whether a  $g_M$  conductance could account for the experimental findings described above. In the model,  $g_M$  was highest within the axon, the SIZ, and the primary neurite connecting the dendritic fields to the SIZ. The dendrites had a lower  $g_M$  density. Although the exact M channel kinetics within the LGMD are uncharacterized, the increased input resistance after  $g_M$  block at both depolarized and hyperpolarized potentials (Fig. 1, B and D) suggests a broad activation range. Accordingly, we chose

activation kinetics with a shallow slope (Fig. 6B). Simulation with different kinetics than those in Fig. 6 were conducted in preliminary simulations. Although most properties described were reproducible in kind by a wide range of channel kinetics, faster channel activation (Fig. 6C) improved the similarity between experimental and simulation data. In these simulations, removal of  $g_M$  reproduced the increase in resting membrane potential (Fig. 6D), input resistance (Fig. 6E), and membrane time constant (Fig. 6F) found in experiments after  $g_M$  blockade by XE991. We simulated current injections with the same time course as the sEPSPs injected experimentally (Fig. 2), and the model also showed increased summation following  $g_M$  blockade (Fig. 6G). The increased summation after  $g_M$  blockade was paired with an increased mean input resistance for the sEPSPs (Fig. 6H).

*Dependence of LGMD spiking mode on  $g_M$  reproduced by LGMD model.* We simulated injection of the same currents used in experiments to induce spiking. As in experimental data, depolarizing current steps produced rhythmic bursting after  $g_M$  removal (Fig. 7A). Similar bursts were also produced by chirp currents (Fig. 7B). Within the model, the bursts were generated by activation of  $Ca^{2+}$  channels close to the SIZ, and the hyperpolarization between bursts was produced by  $Ca^{2+}$ -dependent  $K^+$  channels, in accordance with experimental findings and previous modeling (Dewell and Gabbiani 2018; Peron and Gabbiani 2009a, 2009b). These increased bursts produced a shift in the ISI distribution after  $g_M$  blockade with a larger proportion of spikes having short ISIs (Fig. 7C). The model also exhibited a spike phase progression during the chirp

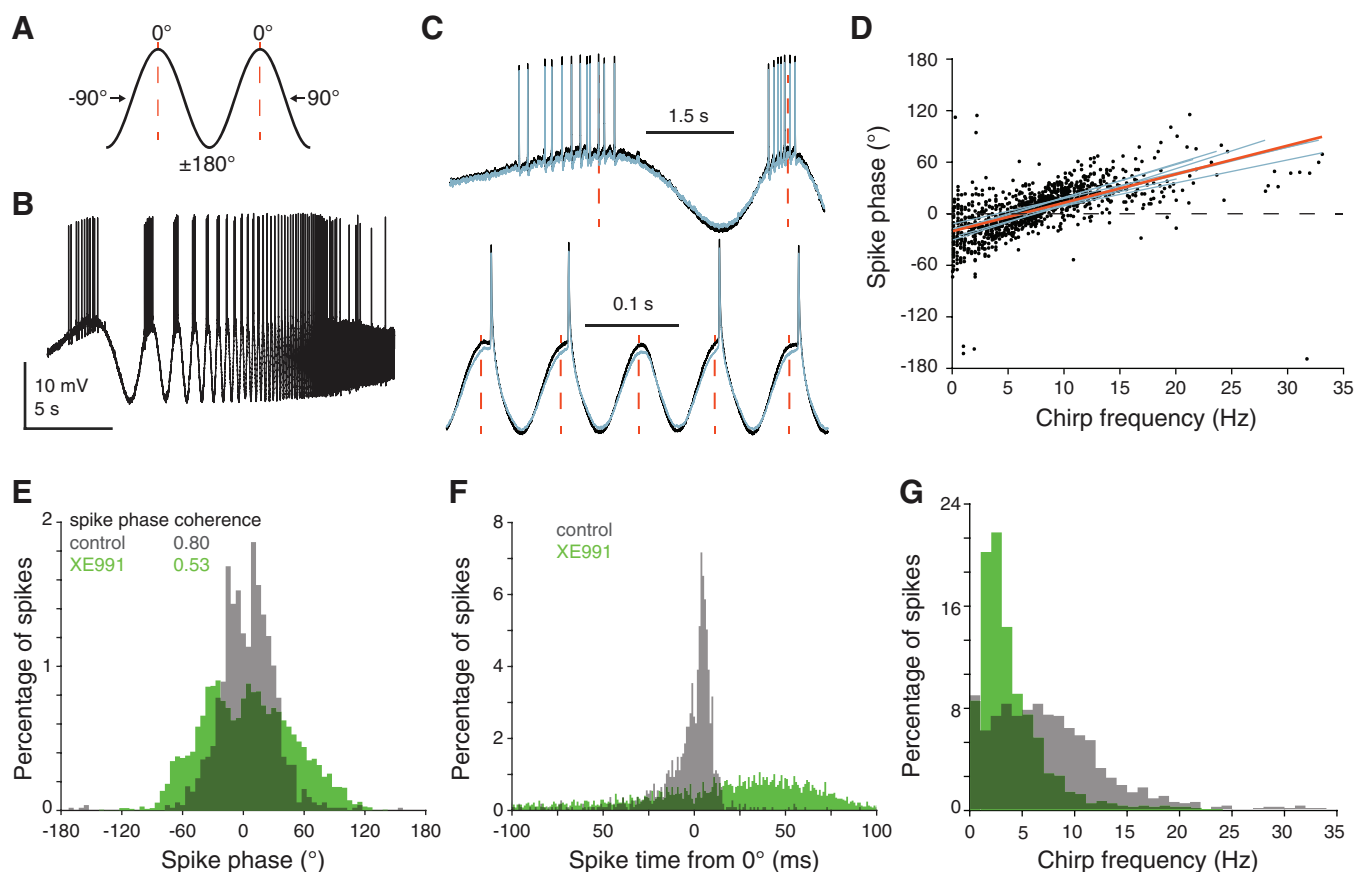


Fig. 4. Reliability of spike timing in the lobula giant movement detector (LGMD) decreased after M channel blockade. **A**: Illustration of the spike phase measurement. Spikes that occurred at the peaks (dashed red lines) and troughs of the input chirp current were considered to be at  $0^\circ$  and  $\pm 180^\circ$ , respectively. Spikes occurring during the rising slope of the current have a negative phase, and those occurring during the falling slope have a positive phase. **B**: an example trace showing high firing elicited by a chirp current superposed on a depolarizing holding current (2 nA). **C**: expanded regions of the same trace as in **B** plus a simultaneous recording from another dendritic location (gray) show spiking during low (top) and high (bottom) input frequencies. Dashed red lines mark  $0^\circ$  phase. At low input frequencies most spikes are generated on the rising (negative) phase, but at high frequencies they come on the falling (positive) phase. The measured spike phase was independent of the recording location (although not necessarily of the current injection location) due to the high synchrony of backpropagating action potentials across dendritic locations. **D**: scatter plot showing the spike phase progression over the chirp current. Linear fits for the population and individual animals are shown in red and blue, respectively, and illustrate the consistency across animals. The  $0^\circ$  phase crossing (dashed line) was  $6.2 \pm 1.2$  Hz. Analysis includes 1,074 spikes from 9 animals ( $r = 0.63$ ,  $P = 5.7 \times 10^{-120}$ ). Red line fit:  $y = a + bx$ , where  $a = -20.4^\circ$  and  $b = 3.33^\circ/\text{Hz}$ . **E**: the spike phase probability distribution for control data (gray bars) shows that spikes cluster around  $0^\circ$  with high phase coherence. If the M current is blocked (green bars; 3,666 spikes from 5 animals), a large reduction in phase coherence is seen ( $P = 1.2 \times 10^{-56}$ ,  $F$ -test). Spike phase coherence was  $>0.65$  for all control animals, and median spike phase was  $5.2^\circ$ . **F**: spike phase was converted to the time domain by dividing by the stimulus frequency (see MATERIALS AND METHODS). This revealed that in control conditions, spikes were grouped near  $0^\circ$ , with 65% within 10 ms of  $0^\circ$  [median  $\pm$  median average deviation (mad) =  $1.95 \pm 5.94$  ms]. After XE991, the spike timing was less consistent and more spikes trailed the input current peak (10% within 10 ms of  $0^\circ$ ; median  $\pm$  mad =  $16.9 \pm 38.1$  ms). **G**: for control data there was no clear preferred frequency for spike generation. After blocking of the M current, a large proportion of spikes were generated at 2–5 Hz.

currents, with most spikes being produced during the rising phase of the input sinusoid at low frequencies but coming on the falling phase at high chirp frequencies (Fig. 7D). For each experiment we visualized the dendritic location of the recording electrode with fluorescent dye and selected model compartments corresponding to the dendritic regions of the experimental recordings. Both experimental and simulated recordings were confined to the region near the base of the excitatory dendritic field. Surprisingly, the spread in the data was higher across locations within the model than it was across animals in our experiments despite the lack of noise sources in the simulations. The LGMD had a spike synchrony frequency of  $6.2 \pm 1.2$  Hz measured across multiple animals, which for the model simulations was  $6.7 \pm 3.8$  Hz measured across dendritic locations (Fig. 7D, blue lines). This increased spread of spike phases resulted in a broader spike phase histogram and lower

spike phase coherence in simulations than in experimental data (Fig. 7E). In both model and experiment,  $g_M$  blockade decreased the reliability of the spike phase and lowered spike phase coherence (Fig. 7E; cf. Fig. 4E). As for spike phase, the time of spiking from the peak of the input current sinusoid was smaller before  $g_M$  block (Fig. 7F; cf. Fig. 4F). That removal of  $g_M$  within the model was sufficient to reproduce the effects of LGMD firing in kind supports the hypothesis that the changes in LGMD firing patterns observed experimentally are primarily intrinsic to the LGMD and not a network phenomenon.

## DISCUSSION

M/Kv7/KCNQ channels influenced both sub- and suprathreshold activity within the LGMD. They increased the reliability of propagation of LGMD activity to downstream motor

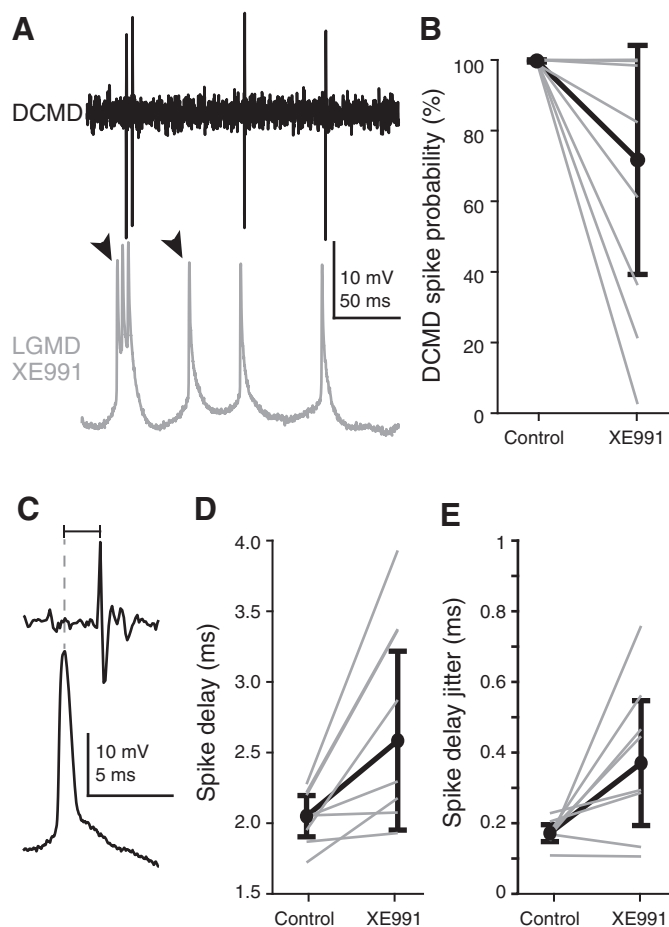


Fig. 5. Blocking M conductance ( $g_M$ ) in the lobula giant movement detector (LGMD) causes failures in descending contralateral movement detector (DCMD) spike initiation. *A*: example trace of a LGMD-DCMD recording pair after  $g_M$  blockade by XE991 (300 mM). Arrowheads mark LGMD spikes that fail to initiate DCMD spikes. *B*: under control conditions, LGMD spikes reliably initiate DCMD spikes (average of 99.7% of LGMD spikes had clear matched DCMD spikes with 1.3- to 4.8-ms delay). After  $g_M$  blockade by XE991, this was substantially reduced. Data from individual animals are displayed with gray lines; 6 of 8 animals had significant reductions in DCMD spike initiations ( $P < 0.05$ ). On average, only 62.7% of LGMD spikes initiated DCMD spikes after  $g_M$  block; black circles and lines are median  $\pm$  median average deviation (mad) of individual percentages. *C*: for LGMD-DCMD spike pairs, the spike delay was measured from the peak of the intracellular LGMD spike (dashed line) to the peak of the extracellular DCMD spike. *D*: in all 8 animals tested, the spike delay significantly increased after  $g_M$  blockade with an average increase of 0.7 ms ( $P < 0.01$ ). Individual animal data are shown in gray; black circles and lines are median  $\pm$  mad of individual means. *E*: in 6 of 8 animals there was also a reduction in the consistency of the spike delay ( $P = 0.039$ , sign rank test) with an average increase in the SD of the spike delay of 0.2 ms ( $P = 0.032$ , paired  $t$ -test).

centers that control escape behaviors, failures of which could have dire consequences for the animal's ability to escape predation. The resting  $g_M$  lowered input resistance, membrane potential, and membrane time constant. This led to decreased amplitude and temporal summation of dendritic inputs that would narrow the temporal window of integration. Additionally, blockade of  $g_M$  caused a change in firing mode, greatly increasing the proportion of burst firing and decreasing spike timing consistency. A single-cell model replicated all effects in kind, if not in exact detail (other than the spike propagation, which would require a multi-cell model), confirming the hypothesis that these are direct changes of the LGMD's intrinsic

properties and not indirectly caused by changes in network activity. Although the results are explainable solely by blockade of an M current, the channel specificity and dosage dependence of XE991 have not been tested under more controlled conditions in grasshoppers. As such, we cannot rule out the possibility that the results presented reflect a blockade of M channels as well as partial blockade of other  $K^+$  channels (see MATERIALS AND METHODS).

Despite combining data from 9 animals, obtained in recordings at 12 different dendritic locations, that caused differing amounts of spiking from chirps in response to different current amplitudes, the population spike phase coherence was high: 0.93 for input frequencies of 5–10 Hz and 0.80 for input frequencies of 0–35 Hz. This is in contrast to pyramidal neurons, where spike phase often changes with recording location, current amplitude, and spike count, a feature believed to play a role in theta spike phase precession (Harris et al. 2002; Magee 2001; McLelland and Paulsen 2009). As in the LGMD, M channel blockade also reduces the consistency of spike phase in hippocampal place cells, which in turn alters spike precession (Kwag et al. 2014). During looming stimuli, the LGMD receives a broad range of input frequencies and amplitudes, yet it generates a firing profile with a consistent time course, independent of the amount of spiking. The consistency of spiking phase independent of the location or amplitude of the input current might thus help the LGMD generate its characteristic looming response profile. Under control conditions, the spike pattern was consistently relayed to the DCMD (Fig. 5*E*), allowing this spike pattern to be accurately conveyed to motor centers.

Somewhat surprisingly, blockade of M channels can result in either an increase or decrease in synaptic release (Huang and Trussell 2011; Shah et al. 2008; Vervaeke et al. 2006). These seemingly contradictory effects are likely due to an increase in RMP both bringing the membrane closer to spike threshold and increasing the resting inactivation of  $Na^+$  channels in the axon and of  $Ca^{2+}$  channels in the synaptic terminals (Battfeld et al. 2014; Greene and Hoshi 2017; Vervaeke et al. 2006). These competing excitatory and inhibitory effects can cause a simultaneous increase in excitability paired with a decrease in spike conduction and synaptic release. Similar effects most likely caused the LGMD-DCMD spike failures (Fig. 5, *A* and *B*). A prolonged increase in RMP in the axon could prevent  $Na^+$  channels from sufficiently de-inactivating to conduct spikes, or a prolonged inactivation of  $Ca^{2+}$  channels might have caused a decrease in synaptic release.

Within our LGMD model, M current blockade increased activation of voltage-gated calcium channels that are localized near the SIZ (Peron and Gabbiani 2009a). These  $Ca^{2+}$  channels generated the spike bursts. The mechanism underlying this burst transition is similar to that found in the interaction between M and persistent  $Na^+$  channels of hippocampal neurons (Golomb et al. 2006). Modeling work has suggested that any channel that produces a slow afterdepolarization following a spike could serve the same role for burst induction (Franci et al. 2018). Following high-frequency spike bursts within the LGMD, there is an increased calcium-dependent  $K^+$  conductance that produces spike frequency adaptation and afterhyperpolarization (Peron and Gabbiani 2009a). During looming stimuli, however, the strength of excitation continually in-

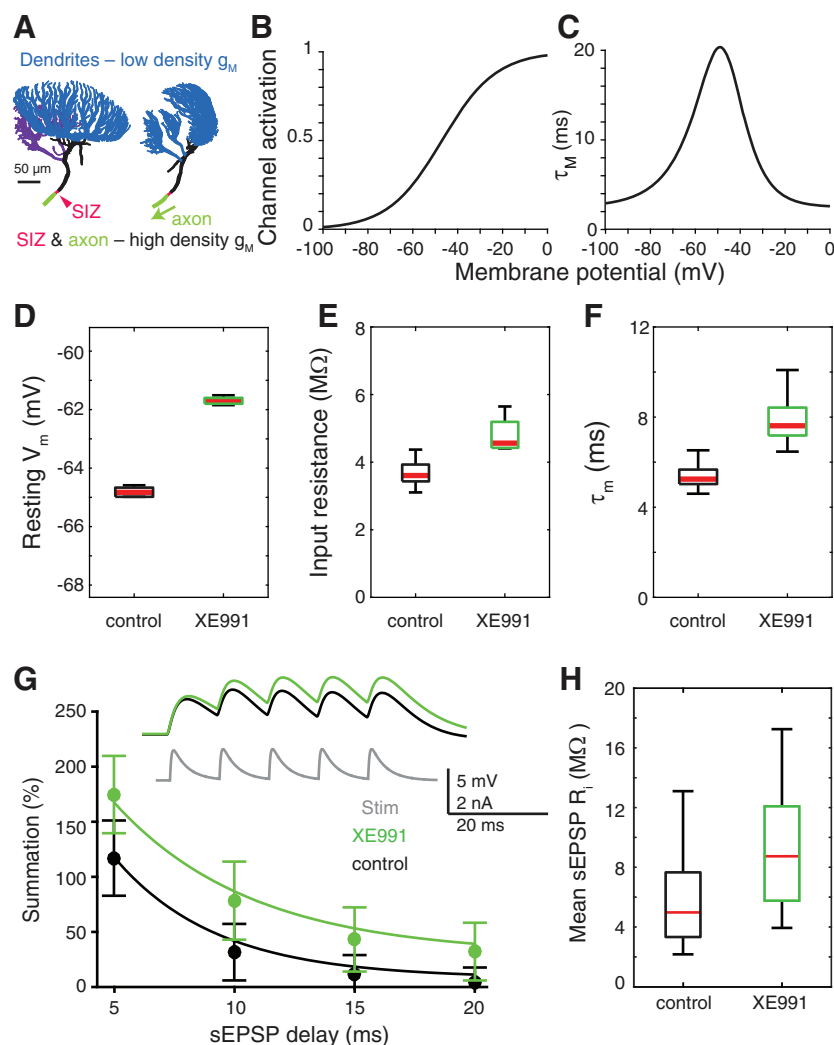


Fig. 6. A multicompartmental model of the lobula giant movement detector (LGMD) reproduced the subthreshold effects of M conductance ( $g_M$ ). *A*: illustration of the model morphology from 2 orientations. The LGMD's 3 dendritic fields (shown in blue) had an average  $g_M$  density of  $26 \mu S/cm^2$  at resting membrane potential ( $V_{rest}$ ;  $-65$  mV). The LGMD's primary neurite (shown in black), which connects the dendritic fields to the spike initiation zone (SIZ; red) and continues because the axon (green) had an average conductance density of  $93 \mu S/cm^2$  at  $V_{rest}$ . The axon extends farther than shown and had a total length of  $463 \mu m$ . *B*: the  $g_M$  value used for simulations had a broad steady-state activation curve with steepness of  $12$  mV. *C*: the time constant of  $g_M$  activation ( $\tau_m$ ) had a minimum and maximum of  $2.5$  and  $21$  ms. *D*: removal of  $g_M$  to simulate XE991 application increased the resting membrane potential (resting  $V_m$ ) by  $2.7$ – $3.5$  mV. For all simulations, data ranges and variability are from measurements of different model sections. *E*: measured input resistance ( $R_i$ ) to step currents increased by  $25$ – $42\%$  after  $g_M$  reduction. *F*: broad steady-state activation curve also increased after simulated XE991 application, by  $41$ – $55\%$ . In *D*–*F*, central lines are medians, top and bottom box edges are  $75$ th and  $25$ th percentiles, and whiskers denote the extent of data. *G*: measured summation to simulated excitatory postsynaptic potentials (sEPSPs) increased for all delays after simulated XE991 application; circles and error bars are medians  $\pm$  mad. *Inset* shows traces of injected current and membrane potential for sEPSPs with delays of  $10$  ms. *H*: median effective  $R_i$  to sEPSPs increased from  $5.0$  to  $8.7 M\Omega$  after  $g_M$  blockade.

creases toward collision, and a strong hyperpolarization is not seen until after the stimulus expansion has stopped.

The initial characterization of the M current was through its suppression by muscarinic acetylcholine receptor activation (Adams and Brown 1982; Delmas and Brown 2005). Since then, many other modulators of M channels have been discovered. The M current can also be suppressed through activation of 5-HT, substance P, glutamate, opioid, and angiotensin receptors (Greene and Hoshi 2017). Conversely, it can be augmented by somatostatin, corticostatin, and dynorphin receptor activation (Greene and Hoshi 2017). These modulators involve numerous different pathways and messengers including phosphatidylinositol 4,5-bisphosphate, inositol (1,4,5)-trisphosphate, PLC, PKC, PKA,  $Ca^{2+}$ , cyclic nucleotides, and tyrosine kinase (Delmas and Brown 2005). The array of modulation effectors suggests that the LGMD's firing mode and spike timing might be dynamically regulated by M channel modulation. Although we do not know which, if any, of these modulatory pathways may be present within the LGMD, conducting all experiments in vivo ensures that the modulation of the channels during our experiments was in a relevant state.

The electrosensory system of weakly electric fish contain looming sensitive pyramidal neurons that share many of the traits described in this review. These neurons respond to

looming objects, have a prominent M current, convey different stimulus aspects in burst and tonic firing, and increase the prevalence of bursting after reduction of the M current (Clarke et al. 2014; Deemyad et al. 2011; Marsat and Pollack 2006). Within these neurons, intrinsic 5-HT modulation can suppress the M current, thereby increasing bursting and excitability while reducing stimulus discriminability (Deemyad et al. 2011). Whether 5-HT-induced M current suppression also alters the spike timing of these neurons has not yet been tested. Within both cortical and hippocampal pyramidal neurons in mammals, M current reduction also induces increased bursting (Battfeld et al. 2014; Golomb et al. 2006; Yue and Yaari 2004). In human neurons, reduced M currents increase neural excitability and bursting, including those in epileptic disorders (Delmas and Brown 2005). Because M current reduction increases burst activity in these disparate species, this suggests that its role in neural regulation is at least in part evolutionarily conserved.

The presynaptic terminals of medullary excitatory afferents to the LGMD possess muscarinic acetylcholine receptors (mAChRs) whose activation leads to lateral excitation, although it is unknown whether activation of these receptors suppresses a presynaptic M current (Rind and Leitinger 2000; Zhu et al. 2018). In our experiments, application of XE991

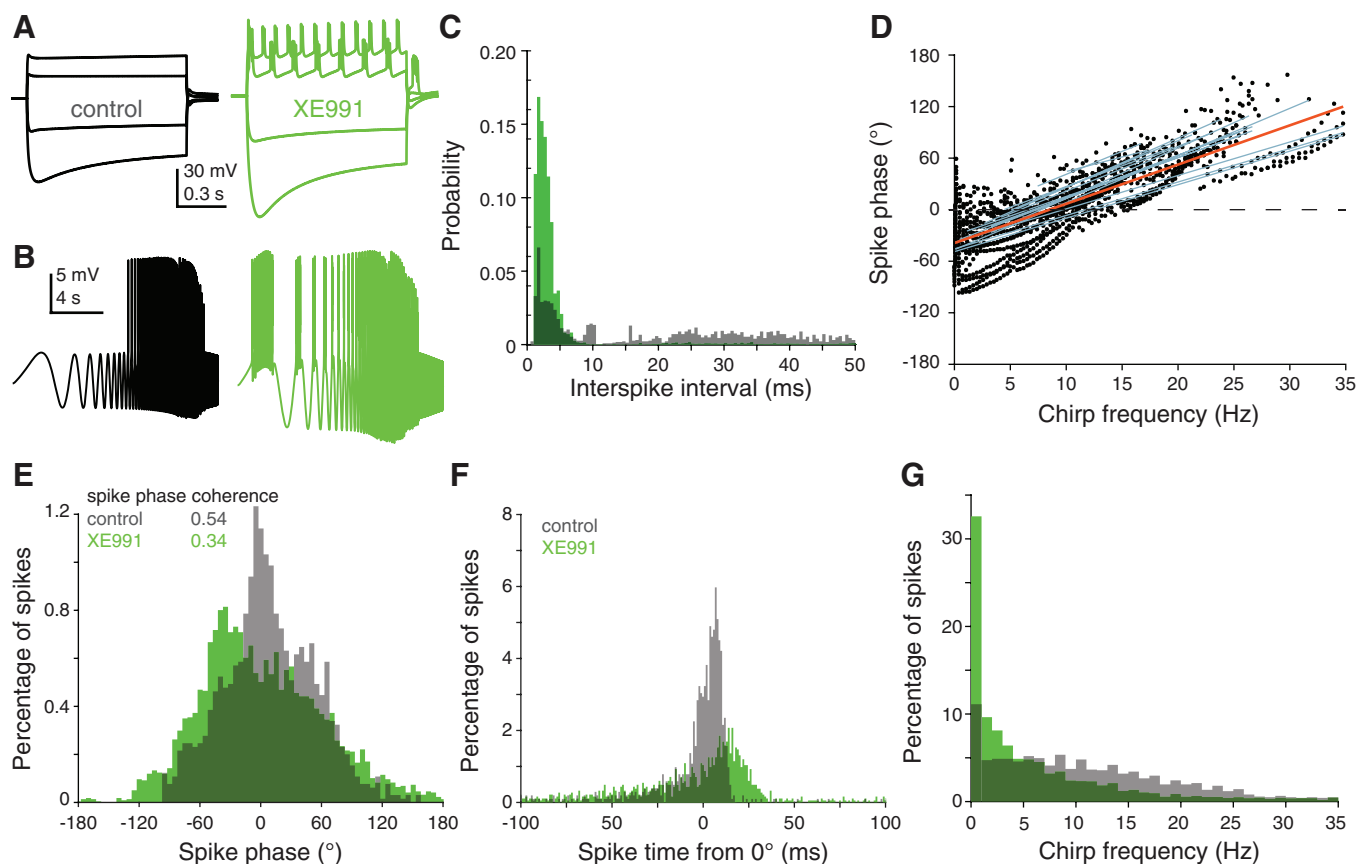


Fig. 7. Model lobula giant movement detector (LGMD) reproduced the role of M conductance ( $g_M$ ) in the LGMD's spiking pattern. *A* and *B*: simulated effect of  $g_M$  blockade on depolarizing current steps (*A*) and chirp currents (*B*) injected into different dendritic sections to induce spiking. For control chirp currents, a constant depolarizing current was superposed (2.5 nA in example trace in *B*, left). *C*: after  $g_M$  blockade, there was a shift in the interspike interval (ISI) distribution, with the proportion of spikes with ISIs of 2–5 ms increasing from 13% to 44%. *D*: as in the experimental data, a spike phase progression occurred with increasing chirp frequency. Data are displayed as in Fig. 4*D* but with each line representing data recorded from different model compartments instead of different recordings. *E*: a broadening of the spike phase distribution produced a 37% reduction in spike phase coherence after  $g_M$  blockade. *F*: the decreased reliability in spike time is shown after conversion of the phase to time from peak current. The spikes occurring within 10 ms of 0° decreased from 62% to 19% after  $g_M$  blockade (compare with Fig. 4*F*). *G*: the model LGMD also produced a shift to a larger percentage of spikes being generated by low-frequency inputs.

reduced excitatory synaptic inputs to the LGMD in all animals, even with local puffing onto the LGMD. This reduced excitatory input cannot have produced any of the effects described in the RESULTS (see MATERIALS AND METHODS). This suggests that there is an M current in presynaptic terminals (or axons) of these medullary afferents and that its blockade by XE991 causes a reduction in synaptic release. Activation of mAChRs has an excitatory effect on synaptic release (Zhu et al. 2018) and, as shown here, XE991 has an inhibitory effect on release from medullary afferents to the LGMD. However, this last result does not exclude the possibility that the mAChR-related excitation is mediated by M current suppression, because XE991 might also cause an increase in the resting inactivation of  $\text{Na}^+$  and  $\text{Ca}^{2+}$  channels, leading to the decreased transmitter release (Battfeld et al. 2014; Huang and Trussell 2011; Schwarz et al. 2006). Indeed, this is likely the cause for the spike propagation failures shown in Fig. 5.

The LGMD has a large dynamic range that allows strong responses to small visual stimuli (Jones and Gabbiani 2010; Rowell et al. 1977) while still selecting between inputs that activate thousands of facets (Dewell and Gabbiani 2018; Gray et al. 2001; Peron and Gabbiani 2009a). This is accomplished through a combination of network and intrinsic properties, including active membrane conductances in the LGMD den-

drites and at the SIZ (Dewell and Gabbiani 2018; Gabbiani and Krapp 2006; Jones and Gabbiani 2010; Peron and Gabbiani 2009a) and regulation of the spike frequency profile and burst spiking (Dewell and Gabbiani 2018; Fotowat and Gabbiani 2007; Gabbiani et al. 2001; McMillan and Gray 2015). The wide dynamic range of the LGMD helps it detect impending danger and collisions both sensitively and selectively. In many neurons, the M current increases the output range through regulation of excitability, spike frequency, and burst firing (Battfeld et al. 2014; Gu et al. 2005; Hu et al. 2007; Lawrence et al. 2006; Schwarz et al. 2006; Shah et al. 2008; Vervaeke et al. 2006; Yue and Yaari 2004). We found that the M current regulates the LGMD's bursting and spike timing, and that it increases the reliability of the signal propagation from the LGMD to downstream motor centers. These results suggest that neuromodulation through M channels or similar ones may play a role in other collision detection circuits, as well.

#### ACKNOWLEDGMENTS

We thank Dr. Ed Cooper for feedback on a previous version of this manuscript.

## GRANTS

This work was supported by National Institute of Mental Health Grant MH-065339 and National Science Foundation Grant IIS-1607518.

## DISCLOSURES

No conflicts of interest, financial or otherwise, are declared by the authors.

## AUTHOR CONTRIBUTIONS

R.B.D. and F.G. conceived and designed research; R.B.D. performed experiments; R.B.D. analyzed data; R.B.D. and F.G. interpreted results of experiments; R.B.D. and F.G. prepared figures; R.B.D. and F.G. drafted manuscript; R.B.D. and F.G. edited and revised manuscript; R.B.D. and F.G. approved final version of manuscript.

## REFERENCES

- Adams PR, Brown DA. Synaptic inhibition of the M-current: slow excitatory post-synaptic potential mechanism in bullfrog sympathetic neurones. *J Physiol* 332: 263–272, 1982. doi:10.1113/jphysiol.1982.sp014412.
- Allen KM, Marsat G. Task-specific sensory coding strategies are matched to detection and discrimination performance. *J Exp Biol* 221: jeb170563, 2018. doi:10.1242/jeb.170563.
- Barrow AJ, Wu SM. Low-conductance HCN1 ion channels augment the frequency response of rod and cone photoreceptors. *J Neurosci* 29: 5841–5853, 2009. doi:10.1523/JNEUROSCI.5746-08.2009.
- Battefeld A, Tran BT, Gavrilis J, Cooper EC, Kole MHP. Heteromeric Kv7.2/7.3 channels differentially regulate action potential initiation and conduction in neocortical myelinated axons. *J Neurosci* 34: 3719–3732, 2014. doi:10.1523/JNEUROSCI.4206-13.2014.
- Brown DA, Adams PR. Muscarinic suppression of a novel voltage-sensitive K<sup>+</sup> current in a vertebrate neurone. *Nature* 283: 673–676, 1980. doi:10.1038/283673a0.
- Cavaliere S, Hodges JLL. Drosophila KCNQ channel displays evolutionarily conserved electrophysiology and pharmacology with mammalian KCNQ channels. *PLoS One* 6: e23898, 2011. doi:10.1371/journal.pone.0023898.
- Clarke SE, Longtin A, Maler L. A neural code for looming and receding motion is distributed over a population of electrosensory ON and OFF contrast cells. *J Neurosci* 34: 5583–5594, 2014. doi:10.1523/JNEUROSCI.4988-13.2014.
- Clarke SE, Longtin A, Maler L. The neural dynamics of sensory focus. *Nat Commun* 6: 8764, 2015. doi:10.1038/ncomms9764.
- Deemyad T, Maler L, Chacron MJ. Inhibition of SK and M channel-mediated currents by 5-HT enables parallel processing by bursts and isolated spikes. *J Neurophysiol* 105: 1276–1294, 2011. doi:10.1152/jn.00792.2010.
- Delmas P, Brown DA. Pathways modulating neural KCNQ/M (Kv7) potassium channels. *Nat Rev Neurosci* 6: 850–862, 2005. doi:10.1038/nrn1785.
- Devaux JJ, Kleopa KA, Cooper EC, Scherer SS. KCNQ2 is a nodal K<sup>+</sup> channel. *J Neurosci* 24: 1236–1244, 2004. doi:10.1523/JNEUROSCI.4512-03.2004.
- Dewell RB, Gabbiani F. Biophysics of object segmentation in a collision-detecting neuron. *eLife* 7: e34238, 2018. doi:10.7554/eLife.34238.
- Elmedy P, Calloe K, Schmitt N, Hansen RS, Grunnet M, Olesen SP. Modulation of ERG channels by XE991. *Basic Clin Pharmacol Toxicol* 100: 316–322, 2007. doi:10.1111/j.1742-7843.2007.00048.x.
- Fotowat H, Gabbiani F. Relationship between the phases of sensory and motor activity during a looming-evoked multistage escape behavior. *J Neurosci* 27: 10047–10059, 2007. doi:10.1523/JNEUROSCI.1515-07.2007.
- Fotowat H, Harrison RR, Gabbiani F. Multiplexing of motor information in the discharge of a collision detecting neuron during escape behaviors. *Neuron* 69: 147–158, 2011. doi:10.1016/j.neuron.2010.12.007.
- Franci A, Drion G, Sepulchre R. Robust and tunable bursting requires slow positive feedback. *J Neurophysiol* 119: 1222–1234, 2018. doi:10.1152/jn.00804.2017.
- Gabbiani F, Krapp HG. Spike-frequency adaptation and intrinsic properties of an identified, looming-sensitive neuron. *J Neurophysiol* 96: 2951–2962, 2006. doi:10.1152/jn.00075.2006.
- Gabbiani F, Mo C, Laurent G. Invariance of angular threshold computation in a wide-field looming-sensitive neuron. *J Neurosci* 21: 314–329, 2001. doi:10.1523/JNEUROSCI.21-01-00314.2001.
- Golomb D, Yue C, Yaari Y. Contribution of persistent Na<sup>+</sup> current and M-type K<sup>+</sup> current to somatic bursting in CA1 pyramidal cells: combined experimental and modeling study. *J Neurophysiol* 96: 1912–1926, 2006. doi:10.1152/jn.00205.2006.
- Gray JR, Lee JK, Robertson RM. Activity of descending contralateral movement detector neurons and collision avoidance behaviour in response to head-on visual stimuli in locusts. *J Comp Physiol A Neuroethol Sens Neural Behav Physiol* 187: 115–129, 2001. doi:10.1007/s003590100182.
- Greene DL, Hoshi N. Modulation of Kv7 channels and excitability in the brain. *Cell Mol Life Sci* 74: 495–508, 2017. doi:10.1007/s00018-016-2359-y.
- Greene DL, Kang S, Hoshi N. XE991 and linopirdine are state-dependent inhibitors for Kv7/KCNQ channels that favor activated single subunits. *J Pharmacol Exp Ther* 362: 177–185, 2017. doi:10.1124/jpet.117.241679.
- Gu N, Vervaeke K, Hu H, Storm JF. Kv7/KCNQ/M and HCN/h, but not K<sub>Ca</sub>2/SK channels, contribute to the somatic medium after-hyperpolarization and excitability control in CA1 hippocampal pyramidal cells. *J Physiol* 566: 689–715, 2005. doi:10.1113/jphysiol.2005.086835.
- Guan D, Higgs MH, Horton LR, Spain WJ, Foehring RC. Contributions of Kv7-mediated potassium current to sub- and suprathreshold responses of rat layer II/III neocortical pyramidal neurons. *J Neurophysiol* 106: 1722–1733, 2011. doi:10.1152/jn.00211.2011.
- Harris KD, Henze DA, Hirase H, Leinekugel X, Dragoi G, Czurkó A, Buzsáki G. Spike train dynamics predicts theta-related phase precession in hippocampal pyramidal cells. *Nature* 417: 738–741, 2002. doi:10.1038/nature00808.
- Hu H, Vervaeke K, Storm JF. M-channels (Kv7/KCNQ channels) that regulate synaptic integration, excitability, and spike pattern of CA1 pyramidal cells are located in the perisomatic region. *J Neurosci* 27: 1853–1867, 2007. doi:10.1523/JNEUROSCI.4463-06.2007.
- Huang H, Trussell LO. KCNQ5 channels control resting properties and release probability of a synapse. *Nat Neurosci* 14: 840–847, 2011. doi:10.1038/nn.2830.
- Jones PW, Gabbiani F. Synchronized neural input shapes stimulus selectivity in a collision-detecting neuron. *Curr Biol* 20: 2052–2057, 2010. doi:10.1016/j.cub.2010.10.025.
- Jones PW, Gabbiani F. Impact of neural noise on a sensory-motor pathway signaling impending collision. *J Neurophysiol* 107: 1067–1079, 2012. doi:10.1152/jn.00607.2011.
- Killmann F, Schürmann FW. Both electrical and chemical transmission between the ‘lobula giant movement detector’ and the ‘descending contralateral movement detector’ neurons of locusts are supported by electron microscopy. *J Neurocytol* 14: 637–652, 1985. doi:10.1007/BF01200802.
- Krahe R, Gabbiani F. Burst firing in sensory systems. *Nat Rev Neurosci* 5: 13–23, 2004. doi:10.1038/nrn1296.
- Kwag J, Jang HJ, Kim M, Lee S. M-type potassium conductance controls the emergence of neural phase codes: a combined experimental and neuron modelling study. *J R Soc Interface* 11: 20140604, 2014. doi:10.1098/rsif.2014.0604.
- Lawrence JJ, Saraga F, Churchill JF, Statland JM, Travis KE, Skinner FK, McBain CJ. Somatodendritic Kv7/KCNQ/M channels control inter-spike interval in hippocampal interneurons. *J Neurosci* 26: 12325–12338, 2006. doi:10.1523/JNEUROSCI.3521-06.2006.
- Lesica NA, Stanley GB. Encoding of natural scene movies by tonic and burst spikes in the lateral geniculate nucleus. *J Neurosci* 24: 10731–10740, 2004. doi:10.1523/JNEUROSCI.3059-04.2004.
- Longden KD, Wicklein M, Hardcastle BJ, Huston SJ, Krapp HG. Spike burst coding of translatory optic flow and depth from motion in the fly visual system. *Curr Biol* 27: 3225–3236.e3, 2017. doi:10.1016/j.cub.2017.09.044.
- Magee JC. Dendritic mechanisms of phase precession in hippocampal CA1 pyramidal neurons. *J Neurophysiol* 86: 528–532, 2001. doi:10.1152/jn.2001.86.1.528.
- Marsat G, Pollack GS. A behavioral role for feature detection by sensory bursts. *J Neurosci* 26: 10542–10547, 2006. doi:10.1523/JNEUROSCI.2221-06.2006.
- Martire M, Castaldo P, D’Amico M, Preziosi P, Annunziato L, Tagliaberta M. M channels containing KCNQ2 subunits modulate norepinephrine, aspartate, and GABA release from hippocampal nerve terminals. *J Neurosci* 24: 592–597, 2004. doi:10.1523/JNEUROSCI.3143-03.2004.
- McLelland D, Paulsen O. Neuronal oscillations and the rate-to-phase transform: mechanism, model and mutual information. *J Physiol* 587: 769–785, 2009. doi:10.1113/jphysiol.2008.164111.
- McMillan GA, Gray JR. Burst firing in a motion-sensitive neural pathway correlates with expansion properties of looming objects that evoke avoidance behaviors. *Front Integr Neurosci* 9: 60, 2015. doi:10.3389/fnint.2015.00060.

- O'Shea M, Williams JL. The anatomy and output connection of a locust visual interneurone; the lobular giant movement detector (LGMD) neurone. *J Comp Physiol* 91: 257–266, 1974. doi:10.1007/BF00698057.
- Peron S, Gabbiani F. Spike frequency adaptation mediates looming stimulus selectivity in a collision-detecting neuron. *Nat Neurosci* 12: 318–326, 2009a. doi:10.1038/nn.2259.
- Peron SP, Gabbiani F. Role of spike-frequency adaptation in shaping neuronal response to dynamic stimuli. *Biol Cybern* 100: 505–520, 2009b. doi:10.1007/s00422-009-0304-y.
- Rind FC. A chemical synapse between two motion detecting neurones in the locust brain. *J Exp Biol* 110: 143–167, 1984.
- Rind FC, Leitinger G. Immunocytochemical evidence that collision sensing neurons in the locust visual system contain acetylcholine. *J Comp Neurol* 423: 389–401, 2000. doi:10.1002/1096-9861(20000731)423:3<389::AID-CNE3>3.0.CO;2-S.
- Rind FC, Simmons PJ. Orthopteran DCMD neuron: a reevaluation of responses to moving objects. I. Selective responses to approaching objects. *J Neurophysiol* 68: 1654–1666, 1992. doi:10.1152/jn.1992.68.5.1654.
- Rowell CH, O'Shea M, Williams JL. The neuronal basis of a sensory analyser, the acridid movement detector system. IV. The preference for small field stimuli. *J Exp Biol* 68: 157–185, 1977.
- Schlotterer GR. Response of the locust descending movement detector neuron to rapidly approaching and withdrawing visual stimuli. *Can J Zool* 55: 1372–1376, 1977. doi:10.1139/z77-179.
- Schwarz JR, Glassmeier G, Cooper EC, Kao T-C, Nodera H, Tabuena D, Kaji R, Bostock H. KCNQ channels mediate  $I_{Ks}$ , a slow  $K^+$  current regulating excitability in the rat node of Ranvier. *J Physiol* 573: 17–34, 2006. doi:10.1113/jphysiol.2006.106815.
- Shah MM, Migliore M, Brown DA. Differential effects of  $K_v7$  (M-) channels on synaptic integration in distinct subcellular compartments of rat hippocampal pyramidal neurons. *J Physiol* 589: 6029–6038, 2011. doi:10.1113/jphysiol.2011.220913.
- Shah MM, Migliore M, Valencia I, Cooper EC, Brown DA. Functional significance of axonal  $K_v7$  channels in hippocampal pyramidal neurons. *Proc Natl Acad Sci USA* 105: 7869–7874, 2008. doi:10.1073/pnas.0802805105.
- Sherman SM. Tonic and burst firing: dual modes of thalamocortical relay. *Trends Neurosci* 24: 122–126, 2001. doi:10.1016/S0166-2236(00)01714-8.
- Sinha M, Narayanan R. HCN channels enhance spike phase coherence and regulate the phase of spikes and LFPs in the theta-frequency range. *Proc Natl Acad Sci USA* 112: E2207–E2216, 2015. doi:10.1073/pnas.1419017112.
- van Brederode JFM, Berger AJ. Spike-firing resonance in hypoglossal motoneurons. *J Neurophysiol* 99: 2916–2928, 2008. doi:10.1152/jn.01037.2007.
- Vervaeke K, Gu N, Agdestein C, Hu H, Storm JF.  $K_v7$ /KCNQ/M-channels in rat glutamatergic hippocampal axons and their role in regulation of excitability and transmitter release. *J Physiol* 576: 235–256, 2006. doi:10.1113/jphysiol.2006.111336.
- Wei AD, Butler A, Salkoff L. KCNQ-like potassium channels in *Caenorhabditis elegans*. Conserved properties and modulation. *J Biol Chem* 280: 21337–21345, 2005. doi:10.1074/jbc.M502734200.
- Wladyka CL, Kunze DL. KCNQ/M-currents contribute to the resting membrane potential in rat visceral sensory neurons. *J Physiol* 575: 175–189, 2006. doi:10.1113/jphysiol.2006.113308.
- Yue C, Yaari Y. KCNQ/M channels control spike afterdepolarization and burst generation in hippocampal neurons. *J Neurosci* 24: 4614–4624, 2004. doi:10.1523/JNEUROSCI.0765-04.2004.
- Zhu Y, Dewell RB, Wang H, Gabbiani F. Pre-synaptic muscarinic excitation enhances the discrimination of looming stimuli in a collision-detection neuron. *Cell Reports* 23: 2365–2378, 2018. doi:10.1016/j.celrep.2018.04.079.

